RESEARCH ARTICLE

MEDICAL PHYSICS

Validation of Monte Carlo ^{131}I radiopharmaceutical dosimetry workflow using a 3D-printed anthropomorphic head and neck phantom

David P. Adam[1] | Joseph J. Grudzinski[2] | Ian Bormett[3] | Benjamin L. Cox[3] | Ian R. Marsh[1] | Tyler J. Bradshaw[2] | Paul M. Harari[4] | Bryan P. Bednarz[1]

[1]Department of Medical Physics, University of Wisconsin-Madison, Madison, Wisconsin, USA

[2]Department of Radiology, University of Wisconsin-Madison, Madison, Wisconsin, USA

[3]Morgridge Institute for Research, University of Wisconsin-Madison, Madison, Wisconsin, USA

[4]Department of Human Oncology, University of Wisconsin-Madison, Madison, Wisconsin, USA

Correspondence
Bryan P. Bednarz, Department of Medical Physics, University of Wisconsin-Madison, 1005 WIMR, 1111 Highland Avenue, Madison, WI 53705, USA.
Email: bbednarz2@wisc.edu

Funding information
Morgridge Institute for Research; NIH National Institute for Dental and Craniofacial Research (NIDCR) and National Cancer Institute (NCI) Specialized Program of Research Excellence (SPORE) Program, Grant/Award Number: P50DE026787; National Cancer Institute, Grant/Award Numbers: U01CA233102-01, P01CA250972; NCI/NIH, Grant/Award Number: T32CA009206

Abstract

Purpose: Approximately 50% of head and neck cancer (HNC) patients will experience loco-regional disease recurrence following initial courses of therapy. Retreatment with external beam radiotherapy (EBRT) is technically challenging and may be associated with a significant risk of irreversible damage to normal tissues. Radiopharmaceutical therapy (RPT) is a potential method to treat recurrent HNC in conjunction with EBRT. Phantoms are used to calibrate and add quantification to nuclear medicine images, and anthropomorphic phantoms can account for both the geometrical and material composition of the head and neck. In this study, we present the creation of an anthropomorphic, head and neck, nuclear medicine phantom, and its characterization for the validation of a Monte Carlo, SPECT image-based, ^{131}I RPT dosimetry workflow.

Methods: 3D-printing techniques were used to create the anthropomorphic phantom from a patient CT dataset. Three ^{131}I SPECT/CT imaging studies were performed using a homogeneous, Jaszczak, and an anthropomorphic phantom to quantify the SPECT images using a GE Optima NM/CT 640 with a high energy general purpose collimator. The impact of collimator detector response (CDR) modeling and volume-based partial volume corrections (PVCs) upon the absorbed dose was calculated using an image-based, Geant4 Monte Carlo RPT dosimetry workflow and compared against a ground truth scenario. Finally, uncertainties were quantified in accordance with recent EANM guidelines.

Results: The 3D-printed anthropomorphic phantom was an accurate re-creation of patient anatomy including bone. The extrapolated Jaszczak recovery coefficients were greater than that of the 3D-printed insert (~22.8 ml) for both the CDR and non-CDR cases (with CDR: 0.536 vs. 0.493, non-CDR: 0.445 vs. 0.426, respectively). Utilizing Jaszczak phantom PVCs, the absorbed dose was underpredicted by 0.7% and 4.9% without and with CDR, respectively. Utilizing anthropomorphic phantom recovery coefficient overpredicted the absorbed dose by 3% both with and without CDR. All dosimetry scenarios that incorporated PVC were within the calculated uncertainty of the activity. The uncertainties in the cumulative activity ranged from 23.6% to 106.4% for Jaszczak spheres ranging in volume from 0.5 to 16 ml.

Conclusion: The accuracy of Monte Carlo-based dosimetry for ^{131}I RPT in HNC was validated with an anthropomorphic phantom. In this study, it was found

that Jaszczak-based PVCs were sufficient. Future applications of the phantom could involve 3D printing and characterizing patient-specific volumes for more personalized RPT dosimetry estimates.

1 | INTRODUCTION

Approximately 50% of head and neck cancer (HNC) patients will experience loco-regional disease recurrence following initial courses of therapy.[1–6] Although many patients can be cured from HNC, the 5-year overall survival rate of patients with locally advanced HNC is approximately 50%,[7] and cure rates have improved only marginally over the last 30 years.[8] Retreatment of HNC is technically challenging and accompanied by a significant risk of irreversible damage to normal tissues that can translate into profound adverse effects on patient health-related quality of life.[9–22] Several studies have ascertained that despite improvement in long term survival (2 years) in approximately 10%–20% of recurrent HNC patients following external beam radiotherapy (EBRT), there is considerable risk for high-grade toxicities after treatment.[9–13,15–23] Despite the ability of EBRT to provide disease control, efforts to reduce the potential of acute and long-term tissue injury in locoregionally recurrent HNC patients following EBRT are clearly warranted.

Radiopharmaceutical therapy (RPT) is one potential treatment that can be combined with EBRT to maintain disease control of recurrent HNC and mitigate high-grade toxicities. RPT involves a biological delivery vector labeled with a radioactive isotope that is designed to preferentially attach to or be internalized by cancer cells. The radioactive drug conjugate is infused directly into a patient's bloodstream allowing it to reach tumor sites located throughout the body. Due to this unique delivery route, the dose-limiting organs are different than EBRT; and, when combined with EBRT, the therapeutic window in the patient can be expanded, potentially allowing physicians to treat more aggressively.

CLR 131,[24] an alkyl phosphocholine (APC) analog with broad cancer targeting abilities, is a promising RPT agent paired to the radioisotope. ^{131}I emits both therapeutic beta particles (mean energy of 606 keV) and diagnostic gamma rays (364 keV), which can be localized using SPECT. APCs enter cells through specialized plasma membrane microdomains called lipid rafts,[24] which are expressed 6–10 times more in cancer cells in comparison to normal tissues. The increased specificity of CLR 131 for malignant cells shows promise for increased therapeutic efficacy in both preclinical and early clinical studies. Preclinical studies confirm pref-erential uptake and retention of CLR 131 in murine HNC xenografts and tumor growth inhibition.[25] Tumor targeting has been observed in patients in on-going and completed clinical trials.[26–28] Additional tumor growth inhibition has been demonstrated when CLR 131 is combined with EBRT.[25]

Given these results, a clinical trial (NCT04105543) is underway at UW-Madison to investigate the efficacy of combining CLR 131 with EBRT with curative intent in treating relapsed HNC.[29] The premise of the trial is to evaluate the combination of CLR 131 and EBRT in the treatment of recurrent HNC, wherein the radiation dose deposited by the CLR 131 permits a dose reduction delivered by EBRT (e.g., standard of care 60–70 Gy will be targeted irrespective of radiation modality). The overall hypothesis of the clinical trial is that the addition of CLR 131 will enable a dose reduction of EBRT, which is safe and tolerable while maintaining favorable tumor response rates and diminishing the adverse impact of radiation treatment on subject-specific symptoms, such as salivary flow, swallowing function, and overall quality of life.

To achieve the objectives of the trial,[30] patient-specific dosimetry is needed to accurately characterize the tumor absorbed dose from CLR 131 at the voxel level. Longitudinal single photon emission computed tomography/computed tomography (SPECT/CT) scans are used to map the time-dependent biodistribution of CLR 131 in the patient and serve as input for voxel-level dosimetry calculations performed by an in-house Monte Carlo-based software called RAPID.[31] The accuracy of the CLR 131 dose calculation depends on the quantitative accuracy of ^{131}I SPECT images. Nuclear medicine phantom scans are used both for quantitative calibration (i.e., convert counts to units of activity) and correction of partial volume effects (PVEs). PVEs, which are dependent on both the size and shape of the structure being imaged,[32–34] are caused by inherent resolution limitations of imaging systems, and can significantly degrade SPECT/CT image quality and quantitative accuracy.

Collimator detector response (CDR) modeling has been recommended by medical internal radiation dosimetry (MIRD) pamphlet 24[35] for SPECT image reconstruction due to septal penetration of high energy ^{131}I photons through the collimator. Without CDR modeling, noise can be quite apparent on reconstructed images, and small structures can be difficult to resolve; however, some have observed Gibbs ringing artifacts

on images reconstructed with CDR enabled, which can affect the resultant activity distribution.[36]

Anthropomorphic nuclear medicine phantoms have been investigated for a variety of organs (kidney,[37–40] liver,[38,40–42] spleen,[38,40] and pancreas[38,39]), but few groups have investigated the use of nuclear medicine head and neck phantoms. 3D-printed head and neck phantoms have been created for CT and MR applications but few for nuclear medicine applications. A prototype head and neck phantom was described by Alqahtani et al. in which the performance of gamma imaging systems was evaluated, but the study did not extend to dosimetry.[43] In these studies, results have generally indicated that anthropomorphic phantoms account for heterogeneities that are not present in traditional nuclear medicine phantoms and are often more accurate than non-anthropomorphic phantoms. 3D-printed anthropomorphic head and neck phantoms that account for the changing contour of the head and neck region and the heterogeneous material composition in the patient have not been investigated. Recently published review articles succinctly demonstrate the state of 3D-printed phantoms.[44,45]

In this work, we aim to validate our image-based RPT dosimetry workflow for the HNC clinical trial with the introduction and characterization of a novel, 3D-printed, anthropomorphic, head and neck nuclear medicine phantom that mimics the geometry and material composition of the head and neck region. Imaging studies will be conducted with both traditional Jaszcazak nuclear medicine phantoms and the anthropomorphic phantom to investigate ^{131}I SPECT/CT calibration, partial volume corrections (PVCs), and the role of CDR modeling on dosimetry. The resultant data from the imaging studies will then be used as input for the ^{131}I RPT dosimetry workflow and compared to ground truth scenarios. Finally, the uncertainties from the imaging studies will be investigated, and the impact of uncertainties on the dosimetry will be discussed.

## 2 | METHODS

2.1 | Phantom creation

The original CT data for the anthropomorphic phantom were accessed from a publicly available database provided by radiation therapy oncology group (RTOG) 0522 study (Figure 1a).[46] The CT data had a voxel resolution of $0.98 \times 0.98 \times 2.4$ mm^3. Important structures such as the tumor, thyroid, lacrimal glands (both left and right), parotid glands (both left and right), and bone were contoured manually using Amira v.5.3.3 (Figure 1b). The labels were then converted to .stl files, which is a file format native to the stereolithography (SL) CAD software created by 3D systems and required for 3D printing. The .stl files were then modified for final assembly using

Magics (Materialise NV, Leuven, Belgium), which is a .stl editing software package (Figure 1c,d). Modifications included the addition of flanges to seal the main volume, the incorporation of mounting points for the assembly of bones and other anatomical features, and ports for filling and sealing the tumor and gland voids.

The final phantom design consisted of nine custom parts, along with commercial hardware for assembly. This included seven 3D-printed pieces, made with two different materials, and two laser-cut acrylic plates. The main chamber (skin) was printed using SL out of Accura60, a proprietary photopolymer resin (3D Systems, Rock Hill, SC, USA), and then clear-coated for water resistance. The thyroid gland was fused to the skin and can be filled independently. The skull and spine were split into three separate parts and printed using SL out of Somos PerFORM, a proprietary photopolymer resin (DSM, Heerlen, Netherlands). The lacrimal glands were fused to the front piece of the skull and can be filled independently. Lastly, the parotid voids and tumor void were printed using SL out of Accura60 (3D Systems) with approximately 2–3-mm wall thickness. The top and bottom of the chamber were formed with quarter inch acrylic plates that were laser-cut to their final size with a PLS6.75 Laser Cutting System (Universal Laser Systems, Scottsdale, AZ, USA). Commercial hardware included o-rings for sealing and nylon bolts for assembly of separate components. The final 3D-printed head-and-neck anthropomorphic phantom is shown in Figure 1e, and a sagittal slice of a CT image of the phantom is depicted in Figure 1f. Table 1 shows the physical material properties taken from material datasheets of the Accura60 and Somos PerFORM comprising the phantom.

2.2 | Phantom studies and SPECT/CT image acquisition

Three phantom studies were conducted, the parameters of which are summarized in Table 2. The first was conducted using a uniform 20-cm cylindrical phantom of volume 5.64 L to calculate the calibration factor to convert the reconstructed SPECT images to units of activity concentration. The second study was with a Jaszczak phantom containing 0.5-, 1-, 2-, 4-, 8-, and 16-ml hollow sphere inserts, with corresponding diameters of 9.9, 12.4, 15.4, 19.8, 24.8, and 31.3 mm, injected with a 9.9:1 insert to background activity concentration and was used to calculate spherical-based recovery coefficients (RCs) for PVC determination. The third study was with the anthropomorphic phantom containing a 22.8-ml tumor insert and injected with a 9.9:1 insert to background activity concentration. The resultant images were used to calculate an anthropomorphic-based recovery coefficient and served as the basis for the image-based RPT dosimetry calculation. SPECT/CT
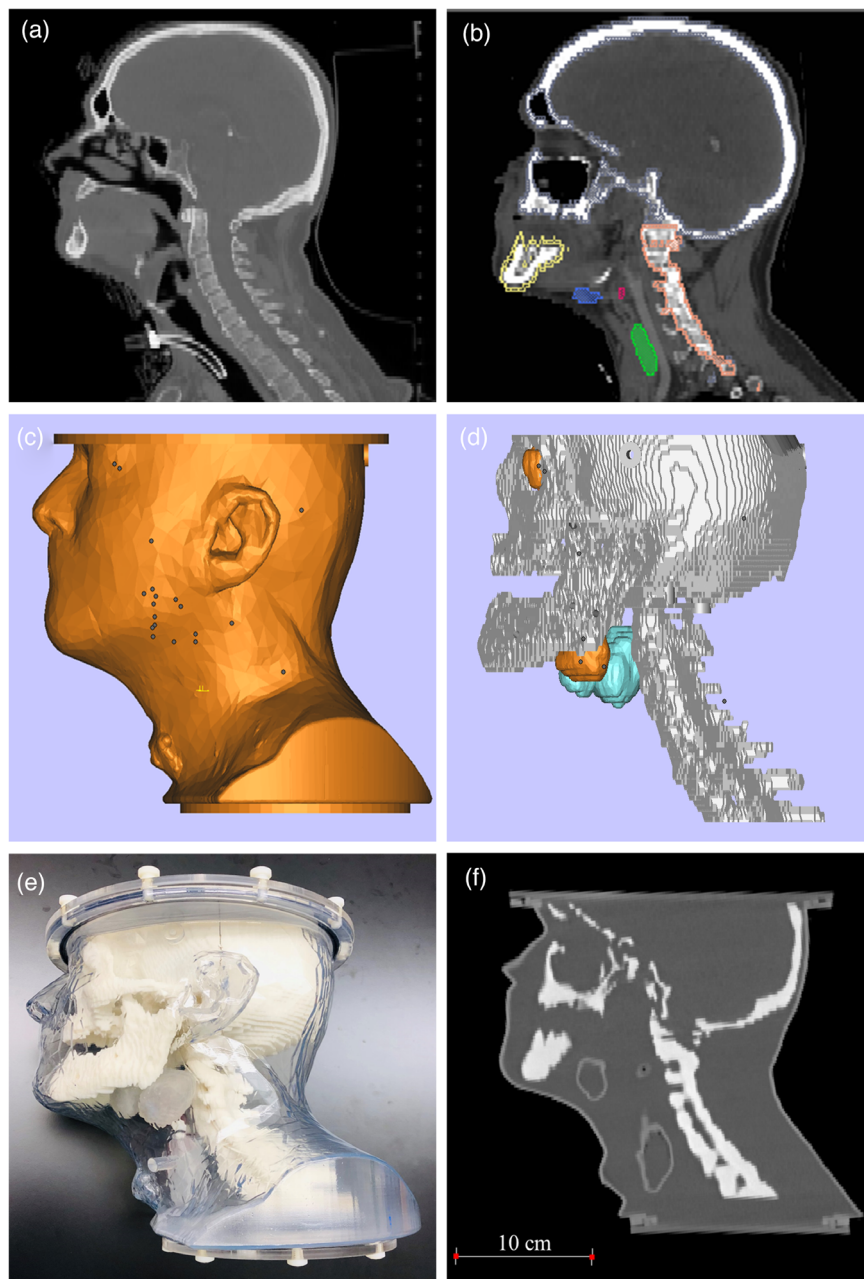
FIGURE 1 Representation of the head and neck (H&N) anthropomorphic phantom development process. (a) Original CT image obtained from a radiation therapy oncology group (RTOG) managed publicly available image repository and (b) relevant contoured structures. (c and d) 3D rendering of patient's skin, bony anatomy, and fillable organ anatomies. (e) Final 3D-printed H&N anthropomorphic phantom. (f) CT image of H&N anthropomorphic phantom

TABLE 1 Physical properties of the bulk materials

Material	Tensile strength (MPa)	Elongation at break (%)	Tensile modulus (MPa)	Flexural strength (MPa)	Water absorption (%)	Hardness (shore D)
Accura60	58–68	5–13	2690–3100	87–101	N/A	86
Somos PerFORM	68–80	1.1–1.2	9800–10500	120–146	0.1–0.2	93–94

Abbreviation: N/A, not applicable.

TABLE 2 Parameters used for SPECT/CT phantom studies

Study	Initial ^{131}I activity concentration (kBq/ml)	Insert to background ratio	Number of frames	Seconds per frame
20-cm cylindrical phantom	105	N/A	120	20
Hot sphere Jaszczak	259	9.9:1	120	60
Anthropomorphic	257	9.9:1	120	60

Abbreviation: N/A, not applicable.

acquisitions were conducted using a GE Optima NM/CT 640 with a high energy general purpose collimator. All images were acquired over 360 degrees into 128×128 pixel matrices per angle. Body contouring was enabled. A photopeak energy window centered at 364 keV and 20% in width (327.6–400.4 keV) and a triple energy window scatter correction with two 20% windows adjacent (267.3–326.7 keV and 401.4–490.6 keV) to the photopeak window were used in the acquisition. A CT was acquired after the SPECT acquisition for CT-derived attenuation corrections (Hawkeye CT, 120 kVp, 20 mA, 487 mAs) and for accurate determination for the location of hot spheres and tumor insert.

Raw image data were reconstructed using the GE Xeleris 4.0 ordered subset expectation maximum algorithm with 10 iterations and 10 subsets with CT-based attenuation correction and both with and without GE's CDR modeling named "resolution recovery" (without: non-RR, with: RR). No postreconstruction filtering was applied. The reconstructed SPECT image matrices were $128 \times 128 \times 128$ voxels with a voxel size of $4.42 \times 4.42 \times 4.42$ mm^3, and the reconstructed CT images had a voxel size of $0.98 \times 0.98 \times 5.0$ mm^3. High-resolution CT images of the anthropomorphic phantom were also acquired using a Siemens SOMATOM Definition Edge (120 kVp, 452 mA, 226 mAs) with a voxel size of $0.977 \times 0.977 \times 2.0$ mm^3. As this high-resolution CT scanner is utilized for photon EBRT treatment planning simulation scans, the scanner is highly characterized, and the electron density CT calibration curve was created utilizing a Gammex 467 Tissue Characterization Phantom.

2.3 | Calculation of calibration factor and recovery coefficients

To convert the recorded SPECT image data into units of activity, the calibration factor, Q, was calculated according to Equation (1),

$$Q = \frac{R}{V \cdot C} \cdot e^{\lambda \Delta t}, \tag{1}$$

where R is the mean count rate of a voxel in a volume of interest (VOI), V is the volume a voxel, C is the activity concentration at the time of syringe measurement, and the last term accounts for physical decay between source preparation time and scan time (Δt).

If R_{voxel} is the count rate in a voxel, then the activity in the voxel, A_{voxel}, is given by Equation (2).

$$A_{\text{voxel}} = \frac{R_{\text{voxel}}}{Q}. \tag{2}$$

To account for PVE, recovery coefficients were calculated according to Equation (3), where the measured activity concentration in the object VOI was determined by quantifying the mean value of each hot insert. Con-

tours for the hot inserts were drawn on the CT, and then the reconstructed SPECT was upsampled using a Lanczos filter to the resolution of the CT and registered to the CT.

$$RC = \frac{\text{Measured activity concentration in object VOI}}{\text{True activity concentration in object VOI}}. \tag{3}$$

To correct the activity in a voxel, the RC is then used in Equation (4), where R_{voxel} is the count rate in the voxel.

$$A_{\text{voxel}} = \frac{R_{\text{voxel}}}{Q \cdot RC}. \tag{4}$$

The recovery coefficients for the Jaszczak spheres were then fit to the function given in Equation (5), where $R_{\text{plateau}}, \beta$, and γ are the curve fitted parameters.[47]

$$RC_{\text{fit}} = R_{\text{plateau}} - \frac{R_{\text{plateau}}}{1 + \left(\frac{V}{\beta}\right)^{\gamma}}. \tag{5}$$

2.4 | Monte Carlo dose calculation

An in-house radiopharmaceutical dosimetry platform called RAPID was used to calculate the mean absorbed dose to the tumor structure in the anthropomorphic phantom.[31] RAPID utilizes nuclear medicine images to define the radionuclide activity in each voxel, and the absorbed dose rate distribution is calculated on the CT, which defines the material composition and mass density of the simulation geometry. The acquired SPECT/CT data from the anthropomorphic phantom study were used to calculate a voxel-level dose rate distribution in the phantom. The dose rate in each voxel was then integrated assuming single timepoint exponential decay to produce a total absorbed dose distribution in the phantom.

Three scenarios were considered: (1) ground truth using a simulated, idealized, SPECT dataset, which was created based upon a segmented CT such that the known activity concentrations were assigned at the voxel level, (2) SPECT-based dosimetry without RCs, and (3) SPECT-based dosimetry with phantom informed RCs. The calibration factor, Q, was applied to the recorded SPECT/CT image of the anthropomorphic phantom. If RCs were utilized, the measured RCs from the Jaszczak phantom and the anthropomorphic phantom were then applied to the anthropomorphic phantom tumor volume to correct the activity concentrations. The resultant dose distributions from the SPECT image-based dosimetry were compared against the separate ground truth scenario, which was run by creating an artificial activity distribution assuming a uniform concentration of 26.2 kBq/cc and 259 kBq/cc in the background and tumor insert, respectively. The SPECT data were

interpolated to the same resolution as the CT. The dose calculation grid was of dimensions $278 \times 280 \times 155$ voxels with a $0.977 \times 0.977 \times 2.00$ mm^3 voxel size. The simulation was run with enough particles (8000 decays per voxel) to ensure Monte Carlo statistical uncertainty below 1.0% in the tumor region. Simulations were run on the University of Wisconsin-Madison Center for High Throughput Computing.

2.5 | Uncertainty analysis

Uncertainty analysis for the activity determination of the Jaszczak phantom study was performed according to the recommended european association of nuclear medicine (EANM) guidelines for determining error propagation in radiopharmaceutical dosimetry.[48]

The fractional uncertainty of the volume determination is given by Equation (6), where a is the voxel size, and D is the equivalent sphere diameter of the contoured structure.

$$\frac{u(v)}{v} = 3\left(\frac{\sqrt{\frac{a^2}{6}}}{D}\right). \tag{6}$$

The uncertainty of the calibration factor (calculated using Equation (1)) is given by Equation (7) and combines in quadrature two components: the assumed 5% error of the radionuclide calibrator activity measurement ($u(A_{cal})$), and the error of the count rate for the scans to determine the calibration factor $u(C_{ref})$, taken to be the standard deviation of the mean count rate for two timepoints.

$$\left[\frac{u(q)}{q}\right]^2 = \left[\frac{u(A_{cal})}{A_{cal}}\right]^2 + \left[\frac{u(C_{ref})}{C_{ref}}\right]^2. \tag{7}$$

The uncertainty of the expression used to fit the recovery coefficient curve (Equation (5)) is given by Equation (8). g_c is a matrix of dimensions 4×1 containing both the partial derivatives of first order of RC with respect to $R_{plateau}$, β, γ, and v, and V_C is a 4×4 matrix containing the covariance matrix from the least-squares fitting process and the uncertainty of the volumes, $u^2(v)$.

$$u^2(RC) = g_c^T V_c g_c \tag{8}$$

The uncertainty in the measured mean counts C associated with the accuracy of the VOI definition is given by Equations (9) and (10),

$$\frac{u(C)}{C} = \frac{\varphi}{2RC}\frac{u(v)}{v} \tag{9}$$

$$\varphi = erf\left(\frac{2r^2}{\sigma\sqrt{2}}\right) - \frac{2\sigma}{r\sqrt{2\pi}}\left[1 - e^{-\frac{2r^2}{\sigma^2}}\right], \tag{10}$$

where r is $D/2$ (the equivalent sphere diameter of the structure), and σ is the standard deviation of the Gaussian point spread function derived from the system spatial resolution, assumed to be 3 mm.[49]

The cumulative activity uncertainties were calculated by adding the system sensitivity, recovery coefficient, and count rate errors in quadrature and subtracting out the covariance of the count rate and recovery coefficient on volume.[35] The uncertainty of the activity was estimated using Equation (11).

$$\left[\frac{u(\tilde{A})}{\tilde{A}}\right]^2 = \left[\frac{u(q)}{q}\right]^2 + \left[\frac{u(RC)}{RC}\right]^2 + \left[\frac{u(C)}{C}\right]^2$$
$$- \frac{\varphi}{RC^2 v}\frac{\partial RC}{\partial v}u^2(v), \tag{11}$$

Estimates of the uncertainty for the anthropomorphic phantom tumor volume were extrapolated from the results of the Jaszczak uncertainties assuming the tumor volume to be spherical.

3 | RESULTS

3.1 | Phantom geometry

Figure 2a–c shows photographs of the head and neck phantom and labels for the fillable and removable inserts. Figure 2a shows an image of the phantom assembled and filled with water. Figure 2b shows the anterior half of the skull insert with the 3D-printed tumor volume and parotid glands attached to it by simple fasteners. Figure 2c shows a side profile of the phantom depicting the lacrimal glad (integrated into the skull) and the thyroid gland (integrated into the shell).
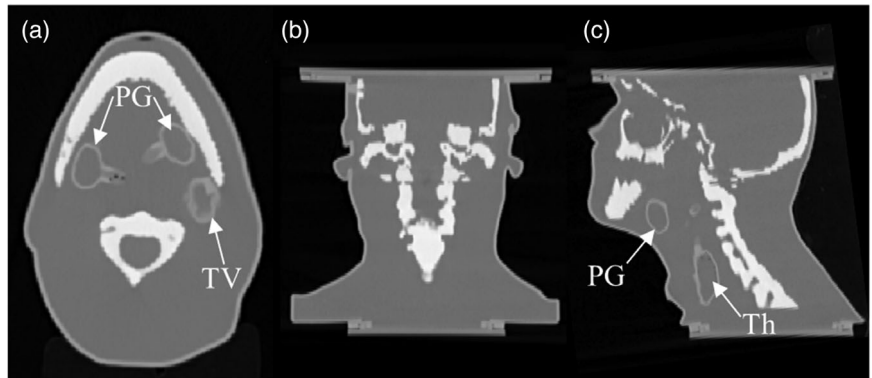
3.2 | Material properties of phantom

Figure 3 shows axial, coronal, and sagittal CT slices of the phantom. Figure 3a shows an axial slice in which the jaw, spine, parotid glands, and tumor volume are present. Figure 3b shows a coronal slice of the phantom in which the skull and the C1-C5 vertebrae are present. Figure 3c depicts a sagittal view of the phantom in which the thyroid gland and the parotid gland are present.

Table 3 provides the radiological properties of the bulk materials. Densities were provided by the manufacturer. The measured hounsfield unit (HU) corresponds to regions of interest (ROIs) drawn on bulk portions
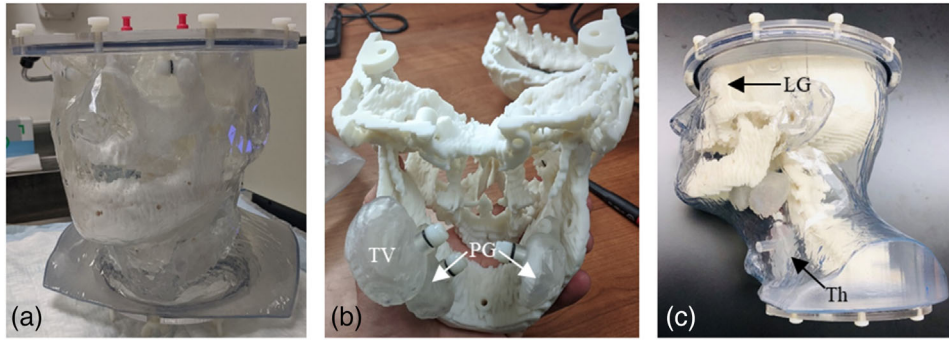
FIGURE 2 Photographs showing the (a) main chamber (skin), (b) lower jawbone assembly, and (c) compiled head and neck phantom. Labels for the fillable inserts including the tumor volume (TV), parotid gland (PG), lacrimal gland (LG), and thyroid (Th) are superimposed on the photographs

FIGURE 3 CT scan of phantom showing (a) axial, (b) coronal, and (c) sagittal views. Labels for the fillable inserts including the tumor volume (TV), parotid gland (PG), and thyroid (Th) are superimposed on the photographs


TABLE 3 Radiological properties of the bulk materials

| Material	Density (g/cc)	Measured HU	Attenuation coefficient (cm⁻¹)		
			^{177}Lu[52]	^{131}I (364 keV)	^{18}F (511 keV)
Accura60	1.21	292.48 +/− 8.57	0.1579	0.1063	0.1068
Somos PerFORM	1.61	876.36 +/− 14.77	0.2137	0.1390	0.1402
Water	1.00	−4.05 +/− 7.95	0.1295	0.0896	0.0896

of the material by the Siemens high-resolution CT scanner. The tabulated attenuation coefficients were computed by utilizing formalisms from the literature, which have calculated a bilinear relationship between measured narrow beam linear attenuation coefficients and Hounsfield units at the photon energies of interest for each isotope. The bilinear relationships were utilized from Brown et al. for ^{131}I,[50] Burger et al. for ^{18}F,[51] and Kabasakal et al. for ^{177}Lu.[52]

Figure 4 depicts a portion of the CT calibration curve for the high-resolution CT scanner that the anthropomorphic phantom was scanned in. It also plots the two 3D-printed materials alongside the curve in which the clinical calibration curve would slightly overpredict the mass density of the material.

Table 4 shows a comparison between the measured volume of fillable chambers in the phantom and the vol-
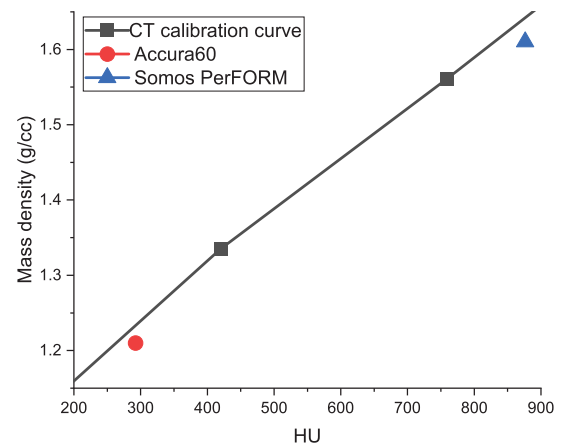
FIGURE 4 Portion of the CT calibration curve for the Siemens high resolution CT scanner, and the 3D-printed materials overlaid
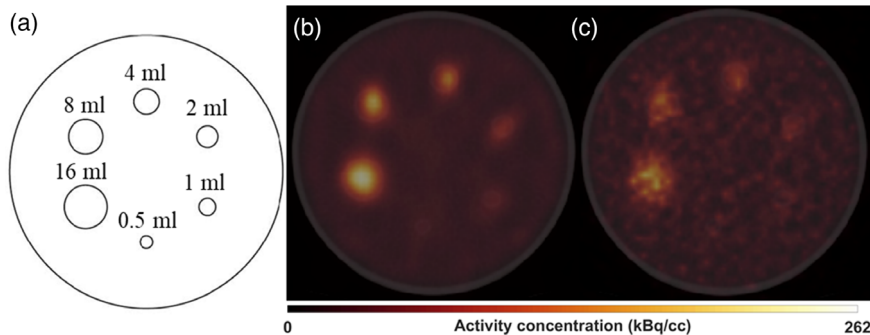
FIGURE 5 (a) Schematic of the spherical inserts for the Jaszczak phantom study and (b) an axial slice of the reconstructed SPECT image with attenuation and scatter correction and superimposed CT of the I-131 scan with resolution recovery (RR) and (c) non-RR

TABLE 4 Comparison of fillable volumes in anthropomorphic phantom (ml)

Fillable void	Measured	DICOM contour	Absolute difference	Percent difference
Parotid$_L$	8.75	8.44	−0.31	−3.54
Parotid$_R$	8.39	8.39	0.00	0.01
Lacrimal$_L$	1.42	1.51	0.09	6.34
Lacrimal$_R$	1.49	1.34	−0.15	−10.07
Thyroid	14.12	15.47	1.35	9.56
GTV	22.77	22.50	−0.27	−1.19

Abbreviations: DICOM, digital imaging and communications in medicine; GTV, gross tumor volume.


FIGURE 6 Recovery coefficients calculated for the Jaszczak phantom and 3D-printed insert as a function of feature size for both resolution recovery (RR) and non-RR

ume of contours made on a high-resolution CT of the phantom. The maximum relative difference between the measured and contour is −10.07% for the right lacrimal gland, which corresponds to an absolute difference of 0.15 ml. The largest absolute difference in volume was for the thyroid gland at 1.35ml. This is likely because it is the most irregularly, aspherical, shaped organ.

3.3 | Phantom imaging studies

Using Equation (1), the calibration factor (Q) was calculated to be 104.2 cps/MBq using RR and 21.4 cps/MBq for non-RR. For the RR case, the average measured activity in the background and tumor compartments were 24.4 kBq/cc and 127.5 kBq/cc, respectively, where the background compartment was a large ROI in the shoulder region containing only water. There was a −6.76% difference between the actual background (26.2 kBq/cc) and measured background. For the non-RR case, the average measured activity in the background and tumor compartments were 24.7 kBq/cc and 110.1 kBq/cc. The difference between the actual background and measured background was −5.81%.

Figure 5 depicts an axial SPECT/CT slice of the Jaszczak phantom after image acquisition and shows the difference in activity recovered with and without resolution recovery. For the RR case, the average mea-

sured activity in the background compartment and 16-ml hot sphere compartments were 26.5 kBq/cc and 133.2 kBq/cc, respectively, and there was a 2.35% difference between the actual background (25.9 kBq/cc) and measured background. For the non-RR case, the average measured activity in the background compartment and 16-ml hot sphere compartments were 26.9 kBq/cc and 109.0 kBq/cc, respectively, and there was a 3.66% difference between the actual background (25.9 kBq/cc) and measured background.

Figure 6 shows the recovery coefficient for the Jaszczak phantom and 3D-printed insert as a function of sphere insert size for both the non-RR and RR cases. As the size of the Jaszczak sphere increased, the recovery coefficients increased. Consistent with theory, the curve fit of the Jaszczak spheres in both cases with the non-RR and RR applied demonstrated that the spheres recovered more activity than the aspherical 3D-printed volume.[34] The Jaszczak phantom results are fitted to the curvefit as in Equation (5), and the 95% confidence bounds for each fit are presented in Figure 6. To calculate the recovery coefficient from the Jaszczak phantom for the anthropomorphic tumor volume, the fitted curve was extrapolated to the volume of the tumor volume.
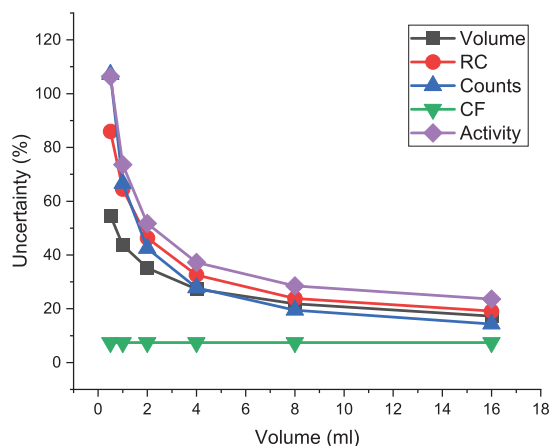
FIGURE 7 Uncertainties from Jaszczak phantom hot spheres study as a function of sphere volume
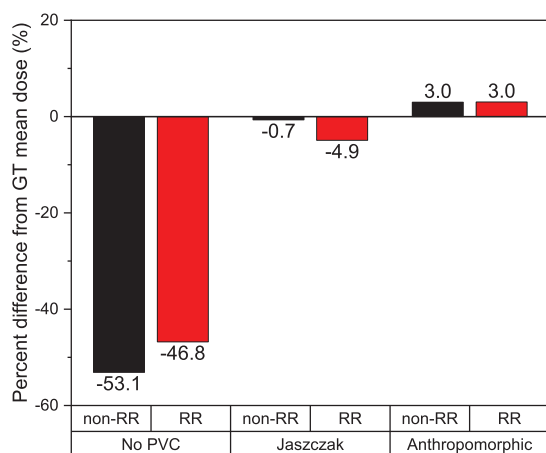
FIGURE 8 Percent difference in mean absorbed dose to the tumor volume compared to the ground truth (GT) scenario of 62.15 Gy for the scenarios considering resolution recovery (RR) and partial volume correction (PVC)

The extrapolated recovery coefficient was greater than that of the 3D-printed insert for both the non-RR and RR cases (with RR: 0.536 vs. 0.493, non-RR: 0.445 vs. 0.426, respectively).

The calculated uncertainties for the RR case of the Jaszczak phantom imaging study are given in Figure 7. The largest uncertainties were the mean counts and RC, which are dependent on the volume determination and the RC fitting function. The range of uncertainties for volume (17.3%–54.7%), RC (19.2%–86.0%), mean counts (14.3%–107.2%), calibration factor (7.47%), and cumulative activity (23.6%–106.4%) were calculated.

3.4 | Monte Carlo dosimetry

Figure 8 shows the difference in the calculated mean tumor dose in comparison to the ground truth scenario with an absorbed dose calculated to be 62.15

Gy. For the RR (non-RR) case, the mean dose to the tumor was underestimated by 46.8% (53.1%) before applying any RC, underestimated by 4.9% (0.7%) after applying a Jaszczak informed RC, and overestimated by 3.0% (3.0%) after applying the 3D-printed insert RC. The extrapolated activity uncertainty estimate from the Jaszczak phantom study presented in Figure 7 for the volume of the tumor was 19.4%; this uncertainty effectively places all PVC dosimetry results within the error estimates.

Figures 9 and 10 shows (a) axial, (b) coronal, and (c) sagittal slices of the absolute absorbed dose rate for the ground truth scenario and the resolution recovery image-based scenario, respectively. Figure 11 depicts the respective relative percent differences calculated between the ground truth and the SPECT-derived activity distributions for the resolution recovery case.

Large dose gradients were present in the RR dosimetry. This is consistent with both spill out due to imaging system limitations and Gibbs ringing artifacts that have been documented when using CDR modeling.[36,53,54] As depicted in relative difference maps in Figure 11, there are stark regions of red, indicating that the SPECT image has much higher dose than the corresponding ground truth. This is attributable to those certain structures like bone material and 3D-printed material were assumed to be impermeable to water, and thus activity was not assigned to them in the ground truth scenario.

4 | DISCUSSION

It was found that, in this study, the Jaszczak-based PVCs were sufficient to correct the activity distributions. While the Jaszczak-derived RC for the non-RR reconstruction was the most accurate scenario, the anthropomorphic phantom derived RC was most accurate for the RR reconstruction, within 3% of the ground truth. The tumor volume studied was quite spherical in shape; it is possible that the disease presentation of patients enrolled in the trial could deviate from spherical behavior in which case the Jaszczak-based recovery coefficients may be less accurate. In the context of uncertainty analysis, the uncertainty in the activity determination was found to be around 23.6% for the 16 ml Jaszczak sphere, and the extrapolated uncertainty estimate for the anthropomorphic tumor volume was 19.4%, placing all the recovered activity dosimetric results within the calculated error and shows that the RCs determined from the anthropomorphic phantom were dosimetrically similar to those derived from the Jaszczak hot sphere phantom. The uncertainties were even higher (up to >100%) for smaller Jaszczak volumes. Uncertainties of this magnitude must be considered and conveyed to physicians for clinical cases. This is consistent with previous work in which VOI delineations have a substantial impact on the activity quantification and dose, which are especially
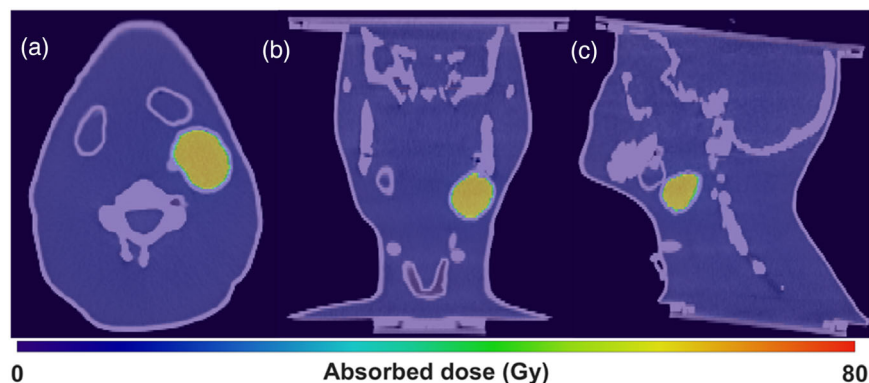
FIGURE 9 Absolute absorbed dose for the ground truth scenario: (a) axial, (b) coronal, and (c) sagittal views
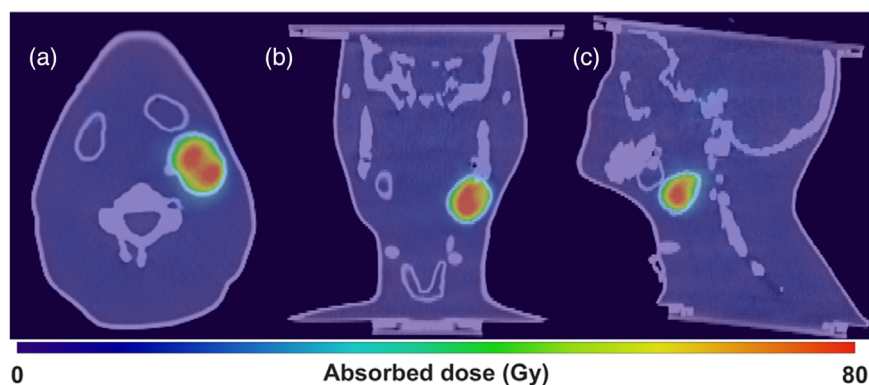
FIGURE 10 Absolute absorbed dose for the resolution recovery scenario: (a) axial, (b) coronal, and (c) sagittal views
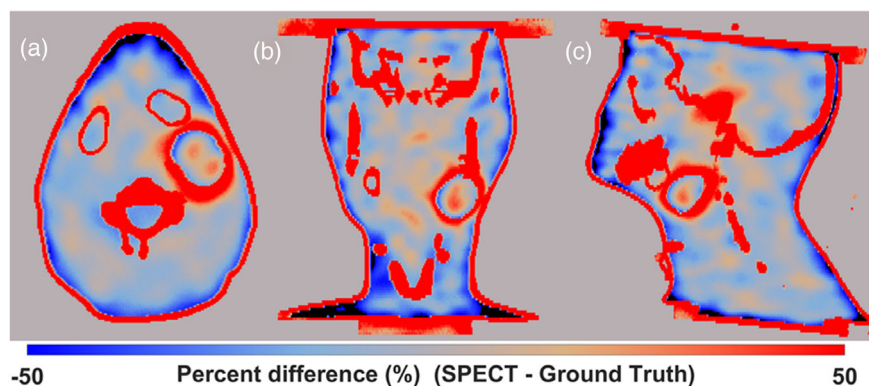
FIGURE 11 Relative dose differences between the ground truth scenario and SPECT-derived activity distribution with resolution recovery for (a) axial, (b) coronal, and (c) sagittal views

important for small structures.[49] Additionally, uncertainties have been reported to be up to 102% for small targets for ^{177}Lu in human clinical trials, placing our results in line with other RPT uncertainties.[55]

Because the calibration factor depends on the accuracy of scatter and attenuation correction, and they vary with phantom geometry,[49] the shape of the phantom can directly affect the accuracy of quantifying activity in the background compartment. This may be the reason for the calibration factor slightly underpredicting the activity concentration in the background compartment (an ROI in the shoulder containing only water) of the anthropomorphic phantom. These types of shape-dependent calibration factors have been previously reported.[38,40] The calibration factor derived from the homogeneous

Jaszczak phantom study was used to keep the anthropomorphic phantom study in line with the imaging parameters and recommended guidelines for upcoming clinical trial patient studies.[35]

In addition to the difference in shape of the phantom's background region, another important distinction of the anthropomorphic phantom is the inclusion of 3D-printed bone-mimicking material, which more resembles the density and corresponding HU of bones in the head and neck to afford a more realistic dosimetric scenario. The bone-type material was measured to have a bulk HU value of 876.36 and density of 1.61 g/cc, which is representative of cortical bone, oftentimes found in the skull. Uncertainties and differences of 3D-printed materials have been demonstrated in previous work

by Craft et.al.[56] In that work, slight differences in density and composition of printed materials resulted in dosimetric differences for clinical photon and electron beams. In the context of ^{131}I RPT dosimetry, not only are dose computations affected because 3D-printed materials may not lie on the CT calibration curve (see Figure 4), but CT-based attenuation corrections for image reconstruction may be affected as well. These material property uncertainties could affect the dosimetry, and the further characterizing of 3D-printed materials should be carefully considered.

RR, the CDR compensation technique included in GE's reconstruction software, Xeleris 4.0[57,58] was investigated because, in theory, high energy photon emissions of ^{131}I requires modeling of the high energy collimators that inherently reduce spatial resolution due to the collimator geometry. We found that there was only a small difference in the dosimetric results between non-RR and RR; however, utilizing RR increased the spatial accuracy of the activity quantification and has been recommended to be used.[35] Additionally, the spatial distribution of activity was less clear and difficult to discern the presence of activity in smaller structures (see Figure 5c) thus limiting its applicability. The CDR model in Xeleris only models the intrinsic and geometric components of the collimator and neglects the collimator scatter and penetration, which can lead to significant higher count recovery for [131]I.[35] In addition to using the manufacturer's RR, Monte Carlo CDR modeling has been studied in previous work to model the CDR explicitly to account for septal penetration and scatter[59,60] and should be considered to improve the accuracy of the image reconstruction.

5 | CONCLUSIONS

The 3D-printed anthropomorphic phantom was created to more accurately represent the geometry and material composition of the head and neck region in comparison to typical non-anthropomorphic Jaszczak-type nuclear medicine phantoms. This phantom was used to evaluate the accuracy of a Monte Carlo, image-based, RPT dosimetry workflow in comparison to a ground truth scenario. We investigated the determination of RCs from different phantoms, the impact of CDR modeling, and assessed the uncertainty in the activity determination. After correcting the reconstructed SPECT images using volume-based RCs, the dosimetry workflow was determined to be accurate within the calculated uncertainty. The Jaszczak-based PVCs were sufficient to correct the activity distributions in this study; however, aspherical volumes may warrant the utilization of anthropomorphic phantom PVC. Further work should characterize the 3D-printed materials rigorously and include Monte Carlo-based reconstructions, which include more accurate CDR modeling.

CONFLICT OF INTEREST

Benjamin L. Cox is a co-founder of Phantech LLC, a manufacturer of imaging phantoms. Bryan Bednarz and Joseph Grudzinski are co-founders and have ownership interest in Voximetry, Inc., a nuclear medicine dosimetry company in Madison, WI. Other authors have no conflict of interest.

ORCID

David P. Adam
https://orcid.org/0000-0002-8282-6660
Ian R. Marsh
https://orcid.org/0000-0002-0031-9746
Tyler J. Bradshaw
https://orcid.org/0000-0001-9549-7002
Bryan P. Bednarz
https://orcid.org/0000-0002-7467-9816

REFERENCES

1. Cognetti DM, Weber RS, Lai SY. Head and neck cancer an evolving treatment paradigm. *Cancer.* 2008;113(7):1911-1932. https://doi.org/10.1002/cncr.23654
2. Forastiere A, Koch W, Trotti A, Sidransky D. Head and Neck Cancer. *N Engl J Med.* 2001;345(26):1890-1900. https://doi.org/10.1056/NEJMra001375
3. Forastiere A, Weber R, Ang K. Treatment of head and neck cancer. *N Engl J Med.* 2008;358(10):1076-1078. https://doi.org/10.1056/NEJMc073274
4. Peters LJ, O'Sullivan B, Giralt J, et al. Critical impact of radiotherapy protocol compliance and quality in the treatment of advanced head and neck cancer: results from TROG 02.02. *J Clin Oncol.* 2010;28(18):2996-3001. https://doi.org/10.1200/JCO.2009.27.4498
5. Pignon JP, le Maître A, Maillard E, Bourhis J. Meta-analysis of chemotherapy in head and neck cancer (MACH-NC): an update on 93 randomised trials and 17346 patients. *Radiother Oncol.* 2009;92(1):4-14. https://doi.org/10.1016/j.radonc.2009.04.014
6. Vokes EE, Weichselbaum RR, Lippman SM, Hong WK. Head and neck cancer. *N Engl J Med.* 1993;328(3):184-194. https://doi.org/10.1056/NEJM199301213280306
7. Pulte D, Brenner H. Changes in survival in head and neck cancers in the late 20th and early 21st century: a period analysis. *Oncologist.* 2010;15(9):994-1001. https://doi.org/10.1634/theoncologist.2009-0289
8. Siegel RL, Miller KD, Jemal A. Cancer statistics, 2015. *CA Cancer J Clin.* 2015;65(1):5-29. https://doi.org/10.3322/caac.21254
9. Chen AM, Phillips TL, Lee NY. Practical considerations in the re-irradiation of recurrent and second primary head-and-neck cancer: who, why, how, and how much? *Int J Radiat Oncol*

Biol Phys. 2011;81(5):1211-1219. https://doi.org/10.1016/j.ijrobp.2011.06.1998

10. Dawson LA, Myers LL, Bradford CR, et al. Conformal re-irradiation of recurrent and new primary head-and-neck cancer. *Int J Radiat Oncol Biol Phys.* 2001;50(2):377-385. https://doi.org/10.1016/S0360-3016(01)01456-0

11. Salama JK, Vokes EE, Chmura SJ, et al. Long-term outcome of concurrent chemotherapy and reirradiation for recurrent and second primary head-and-neck squamous cell carcinoma. *Int J Radiat Oncol Biol Phys.* 2006;64(2):382-391. https://doi.org/10.1016/j.ijrobp.2005.07.005

12. Spencer SA, Harris J, Wheeler RH, et al. RTOG 96-10: reirradiation with concurrent hydroxyurea and 5-fluorouracil in patients with squamous cell cancer of the head and neck. *Int J Radiat Oncol Biol Phys.* 2001;51(5):1299-1304. https://doi.org/10.1016/S0360-3016(01)01745-X

13. Stevens KR, Britsch A, Moss WT. High-dose reirradiation of head and neck cancer with curative intent. *Int J Radiat Oncol Biol Phys.* 1994;29(4):687-698. https://doi.org/10.1016/0360-3016(94)90555-X

14. Connor NP, Cohen SB, Kammer RE, et al. Impact of conventional radiotherapy on health-related quality of life and critical functions of the head and neck. *Int J Radiat Oncol Biol Phys.* 2006;65(4):1051-1062. https://doi.org/10.1016/j.ijrobp.2006.01.054

15. De Crevoisier R, Bourhis J, Domenge C, et al. Full-dose reirradiation for unresectable head and neck carcinoma: experience at the Gustave-Roussy Institute in a series of 169 patients. *J Clin Oncol* 1998;16(11):3556-3562. https://doi.org/10.1200/JCO.1998.16.11.3556

16. Hehr T, Classen J, Belka C, et al. Reirradiation alternating with docetaxel and cisplatin in inoperable recurrence of head-and-neck cancer: a prospective phase I/II trial. *Int J Radiat Oncol Biol Phys.* 2005;61(5):1423-1431. https://doi.org/10.1016/j.ijrobp.2004.08.020

17. Hoebers F, Heemsbergen W, Moor S, et al. Reirradiation for head-and-neck cancer: delicate balance between effectiveness and toxicity. *Int J Radiat Oncol Biol Phys.* 2011;81(3):e111-e118. https://doi.org/10.1016/j.ijrobp.2011.01.004

18. Kasperts N, Slotman B, Leemans CR, Langendijk JA. A review on re-irradiation for recurrent and second primary head and neck cancer. *Oral Oncol.* 2005;41(3):225-243. https://doi.org/10.1016/j.oraloncology.2004.07.006

19. Kramer NM, Horwitz EM, Cheng J, et al. Toxicity and outcome analysis of patients with recurrent head and neck cancer treated with hyperfractionated split-course reirradiation and concurrent cisplatin and paclitaxel chemotherapy from two prospective phase I and II studies. *Head Neck.* 2005;27(5):406-414. https://doi.org/10.1002/hed.20163

20. Langer CJ, Harris J, Horwitz EM, et al. Phase II study of low-dose paclitaxel and cisplatin in combination with split-course concomitant twice-daily reirradiation in recurrent squamous cell carcinoma of the head and neck: results of radiation therapy oncology group protocol 9911. *J Clin Oncol.* 2007;25(30):4800-4805. https://doi.org/10.1200/JCO.2006.07.9194

21. Mendenhall WM, Mendenhall CM, Malyapa RS, Palta JR, Mendenhall NP. Re-irradiation of head and neck carcinoma. *Am J Clin Oncol.* 2008;31(4):393-398. https://doi.org/10.1097/COC.0b013e3181637398

22. Nag S, Schuller DE, Martinez-Monge R, Rodriguez-Villalba S, Grecula J, Bauer C. Intraoperative electron beam radiotherapy for previously irradiated advanced head and neck malignancies. *Int J Radiat Oncol Biol Phys.* 1998;42(5):1085-1089. https://doi.org/10.1016/S0360-3016(98)00289-2

23. Spencer S, Wheeler R, Peters G, et al. Phase 1 trial of combined chemotherapy and reirradiation for recurrent unresectable head and neck cancer. *Head Neck.* 2003;25(2):118-122. https://doi.org/10.1002/hed.10178

24. Weichert JP, Clark PA, Kandela IK, et al. Alkylphosphocholine analogs for broad-spectrum cancer imaging and therapy. *Sci Transl Med.* 2014;6(240):240ra75-240ra75. https://doi.org/10.1126/scitranslmed.3007646

25. Morris ZS, Weichert JP, Saker J, et al. Therapeutic combination of radiolabeled CLR1404 with external beam radiation in head and neck cancer model systems. *Radiotherapy and Oncology*. Elsevier Ireland Ltd; 2015:504-509. https://doi.org/10.1016/j.radonc.2015.06.015

26. Grudzinski JJ, Titz B, Kozak K, et al. A phase 1 study of 131I-CLR1404 in patients with relapsed or refractory advanced solid tumors: dosimetry, biodistribution, pharmacokinetics, and safety. *PLoS One.* 2014;9(11):e111652. https://doi.org/10.1371/journal.pone.0111652

27. Deming DA, Maher ME, Leystra AA, et al. Phospholipid ether analogs for the detection of colorectal tumors. *PLoS One.* 2014;9(10):e109668. https://doi.org/10.1371/journal.pone.0109668

28. Lubner SJ, Mullvain J, Perlman S, et al. A phase 1, multi-center, open-label, dose-escalation study of 131I-CLR1404 in subjects with relapsed or refractory advanced solid malignancies. *Cancer Invest.* 2015;33(10):483-489. https://doi.org/10.3109/07357907.2015.1081691

29. CLR 131 Combined With Radiation for Head and Neck Cancer. clinicaltrials.gov. Accessed May 3, 2020. https://clinicaltrials.gov/ct2/show/NCT04105543

30. WAHL R. The clinical importance of dosimetry in radioimmunotherapy with tositumomab and iodine I 131 tositumomab. *Semin Oncol.* 2003;30(2):31-38. https://doi.org/10.1016/S0093-7754(03)70055-4

31. Besemer AE, Yang YM, Grudzinski JJ, Hall LT, Bednarz BP. Development and validation of RAPID: a patient-specific Monte Carlo three-dimensional internal dosimetry platform. *Cancer Biother Radiopharm.* 2018;33(4):155-165. https://doi.org/10.1089/cbr.2018.2451

32. Soret M, Bacharach SL, Buvat I. Partial-volume effect in PET tumor imaging. *J Nucl Med.* 2007;48(6):932-945. https://doi.org/10.2967/jnumed.106.035774

33. Hoffman EJ, Huang S-C, Phelps ME. Quantitation in positron emission computed tomography. *J Comput Assist Tomogr.* 1979;3(3):299-308. https://doi.org/10.1097/00004728-197906000-00001

34. Dewaraja YK, Ljungberg M, Koral KF. Monte Carlo evaluation of object shape effects in iodine-131 SPET tumor activity quantification. *Eur J Nucl Med.* 2001;28(7):900-906. https://doi.org/10.1007/s002590100551

35. Dewaraja YK, Ljungberg M, Green AJ, et al. MIRD pamphlet no. 24: guidelines for quantitative 131I SPECT in dosimetry applications. *J Nucl Med.* 2013;54(12):2182-2188. https://doi.org/10.2967/jnumed.113.122390

36. Erlandsson K, Buvat I, Pretorius PH, Thomas BA, Hutton BF. A review of partial volume correction techniques for emission tomography and their applications in neurology, cardiology and oncology. *Phys Med Biol.* 2012;57(21):R119-R159. https://doi.org/10.1088/0031-9155/57/21/R119

37. Tran-Gia J, Lassmann M. Optimizing image quantification for 177Lu SPECT/CT based on a 3D printed 2-compartment kidney phantom. *J Nucl Med.* 2018;59(4):616-624. https://doi.org/10.2967/jnumed.117.200170

38. Robinson AP, Tipping J, Cullen DM, et al. Organ-specific SPECT activity calibration using 3D printed phantoms for molecular radiotherapy dosimetry. *EJNMMI Phys.* 2016;3(1):12. https://doi.org/10.1186/s40658-016-0148-1

39. Woliner-van der Weg W, Deden LN, Meeuwis APW, et al. A 3D-printed anatomical pancreas and kidney phantom for optimizing SPECT/CT reconstruction settings in beta cell imaging using 111In-exendin. *EJNMMI Phys.* 2016;3(1):29. https://doi.org/10.1186/s40658-016-0165-0

40. Price E, Robinson AP, Cullen DM, et al. Improving molecular radiotherapy dosimetry using anthropomorphic calibration. *Phys Medica.* 2019;58:40-46. https://doi.org/10.1016/j.ejmp.2019.01.013

41. Gear JI, Cummings C, Craig AJ, et al. Abdo-Man: a 3D-printed anthropomorphic phantom for validating quantitative SIRT. *EJNMMI Phys.* 2016;3(1):17. https://doi.org/10.1186/s40658-016-0151-6

42. D'Arienzo M, Pimpinella M, Capogni M, et al. Phantom validation of quantitative Y-90 PET/CT-based dosimetry in liver radioembolization. *EJNMMI Res.* 2017;7(1):94. https://doi.org/10.1186/s13550-017-0341-9

43. Alqahtani MS, Lees JE, Bugby SL, Samara-Ratna P, Ng AH, Perkins AC. Design and implementation of a prototype head and neck phantom for the performance evaluation of gamma imaging systems. *EJNMMI Phys.* 2017;4(1):19. https://doi.org/10.1186/s40658-017-0186-3

44. Filippou V, Tsoumpas C. Recent advances on the development of phantoms using 3D printing for imaging with CT, MRI, PET, SPECT, and ultrasound. *Med Phys.* 2018;45(9):e740-e760. https://doi.org/10.1002/mp.13058

45. Tino R, Yeo A, Leary M, Brandt M, Kron T. A systematic review on 3D-Printed imaging and dosimetry phantoms in radiation therapy. *Technol Cancer Res Treat.* 2019;18:1-14. https://doi.org/10.1177/1533033819870208

46. Ang KK, Zhang Q, Rosenthal DI, et al. Randomized phase III trial of concurrent accelerated radiation plus cisplatin with or without cetuximab for stage III to IV head and neck carcinoma: RTOG 0522. *J Clin Oncol.* 2014;32(27):2940-2950. https://doi.org/10.1200/JCO.2013.53.5633

47. Taprogge J, Leek F, Schurrat T, et al. Setting up a quantitative SPECT imaging network for a European multi-centre dosimetry study of radioiodine treatment for thyroid cancer as part of the MEDIRAD project. *EJNMMI Phys.* 2020;7(1):61. https://doi.org/10.1186/s40658-020-00332-9

48. Gear JI, Cox MG, Gustafsson J, et al. EANM practical guidance on uncertainty analysis for molecular radiotherapy absorbed dose calculations. *Eur J Nucl Med Mol Imaging.* 2018;45(13):2456-2474. https://doi.org/10.1007/s00259-018-4136-7

49. Gregory RA, Murray I, Gear J, et al. Standardised quantitative radioiodine SPECT/CT imaging for multicentre dosimetry trials in molecular radiotherapy. *Phys Med Biol.* 2019;64(24):245013. https://doi.org/10.1088/1361-6560/ab5b6c

50. Brown S, Bailey DL, Willowson K, Baldock C. Investigation of the relationship between linear attenuation coefficients and CT Hounsfield units using radionuclides for SPECT. *Appl Radiat Isot.* 2008;66(9):1206-1212. https://doi.org/10.1016/j.apradiso.2008.01.002

51. Burger C, Goerres G, Schoenes S, Buck A, Lonn A, Von Schulthess G. PET attenuation coefficients from CT images: experimental evaluation of the transformation of CT into PET 511-keV attenuation coefficients. *Eur J Nucl Med.* 2002;29(7):922-927. https://doi.org/10.1007/s00259-002-0796-3

52. Kabasakal L, AbuQbeitah M, Aygün A, et al. Pre-therapeutic dosimetry of normal organs and tissues of 177Lu-PSMA-617 prostate-specific membrane antigen (PSMA) inhibitor in patients with castration-resistant prostate cancer. *Eur J Nucl Med Mol Imaging.* 2015;42(13):1976-1983. https://doi.org/10.1007/s00259-015-3125-3

53. Ljungberg M, Sjögren-Gleisner K. The accuracy of absorbed dose estimates in tumours determined by quantitative SPECT: a Monte Carlo study. *Acta Oncol (Madr).* 2011;50(6):981-989. https://doi.org/10.3109/0284186X.2011.584559

54. Kangasmaa T, Sohlberg A, Kuikka JT. Reduction of collimator correction artefacts with bayesian reconstruction in spect. *Int J Mol Imaging.* 2011;2011:1-6. https://doi.org/10.1155/2011/630813

55. Finocchiaro D, Gear JI, Fioroni F, et al. Uncertainty analysis of tumour absorbed dose calculations in molecular radiotherapy. *EJNMMI Phys.* 2020;7(1):63. https://doi.org/10.1186/s40658-020-00328-5

56. Craft DF, Kry SF, Balter P, Salehpour M, Woodward W, Howell RM. Material matters: analysis of density uncertainty in 3D printing and its consequences for radiation oncology. *Med Phys.* 2018;45(4):1614-1621. https://doi.org/10.1002/mp.12839

57. Tsui BMW, Hu H-B, Gilland DR, Gullberg GT. Implementation of simultaneous attenuation and detector response correction in SPECT. *IEEE Trans Nucl Sci.* 1988;35(1):778-783. https://doi.org/10.1109/23.12831

58. Tsui BMW, Frey EC, Zhao X, Lalush DS, Johnston RE, McCartney WH. The importance and implementation of accurate 3D compensation methods for quantitative SPECT. *Phys Med Biol.* 1994;39(3):509-530. https://doi.org/10.1088/0031-9155/39/3/015

59. Dewaraja YK, Ljungberg M, Koral KF. Characterization of scatter and penetration using Monte Carlo simulation in 131I imaging. *J Nucl Med.* 2000;41(1):123-130.

60. Autret D, Bitar A, Ferrer L, Lisbona A, Bardiès M. Monte Carlo modeling of gamma cameras for I-131 imaging in targeted radiotherapy. *Cancer Biother Radiopharm.* 2005;20(1):77-84. https://doi.org/10.1089/cbr.2005.20.77